Journal of Colloid and Interface Science 665 (2024) 355–364

Contents lists available at ScienceDirect

Journal of Colloid And Interface Science

journal homepage: www.elsevier.com/locate/jcis

Regular Article

Heterogeneous engineering and carbon confinement strategy to synergistically boost the sodium storage performance of transition metal selenides

Peng Wang [a], Xiangyue Liao [a], Min Xie [a], Qiaoji Zheng [a], Yuxiang Chen [a], Kwok-Ho Lam [c,*], Heng Zhang [b,*], Dunmin Lin [a,*]

[a] College of Chemistry and Materials Science, Sichuan Normal University, Chengdu 610066, China
[b] School of Materials Science and Engineering, Suzhou University of Science and Technology, Suzhou 215009, China
[c] Centre for Medical and Industrial Ultrasonics, James Watt School of Engineering, University of Glasgow, Glasgow, Scotland, U.K

GRAPHICAL ABSTRACT

The redistribution of electrons is driven by the electric field at the heterogeneous interface, optimizing the electronic structure of the anode material and improving the reaction kinetics. This optimization contributes to the enhanced sodium storage performance of transition metal selenides with the dual-carbon-confined strategy.

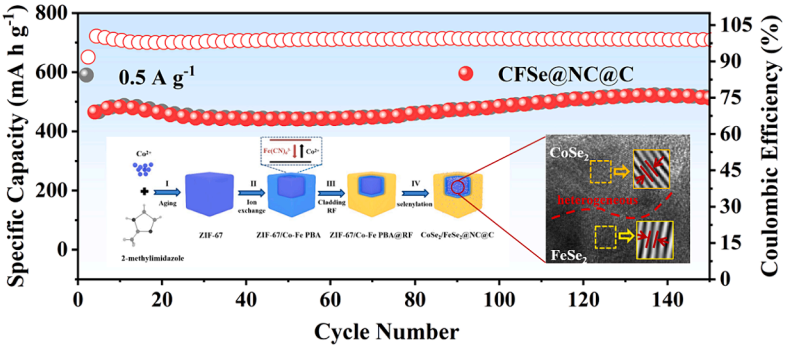

ARTICLE INFO

Keywords:
Sodium-ion batteries
Transition metal selenides
ZIF-67
Nanocubes
Heterogeneous interface
Carbon confinement

ABSTRACT

Transition metal selenides (TMSs) stand out as a promising anode material for sodium-ion batteries (SIBs) owing to their natural resources and exceptional sodium storage capacity. Despite these advantages, their practical application faces challenges, such as poor electronic conductivity, sluggish reaction kinetics and severe agglomeration during electrochemical reactions, hindering their effective utilization. Herein, the dual-carbon-confined $CoSe_2/FeSe_2$@NC@C nanocubes with heterogeneous structure are synthesized using ZIF-67 as the template by ion exchange, resorcin-formaldehyde (RF) coating, and subsequent *in situ* carbonization and selenidation. The *N*-doped porous carbon promotes rapid electrolyte penetration and minimizes the agglomeration of active materials during charging and discharging, while the RF-derived carbon framework reduces the cycling stress and keeps the integrity of the material structure. More importantly, the built-in electric field at the heterogeneous boundary layer drives electron redistribution, optimizing the electronic structure and enhancing the reaction kinetics of the anode material. Based on this, the nanocubes of $CoSe_2/FeSe_2$@NC@C exhibits superb

* Corresponding authors.
E-mail addresses: kwokho.lam@glasgow.ac.uk (K.-H. Lam), zhangheng@usts.edu.cn (H. Zhang), ddmd222@sicnu.edu.cn (D. Lin).

https://doi.org/10.1016/j.jcis.2024.03.107
Received 21 December 2023; Received in revised form 12 March 2024; Accepted 15 March 2024
Available online 16 March 2024

sodium storage performance, delivering a high discharge capacity of 512.6 mA h g^{-1} at 0.5 A g^{-1} after 150 cycles and giving a discharge capacity of 298.2 mA h g^{-1} at 10 A g^{-1} with a CE close to 100.0 % even after 1000 cycles. This study proposes a viable method to synthesize advanced anodes for SIBs by a synergy effect of heterogeneous interfacial engineering and a carbon confinement strategy.

1. Introduction

In recent years, the growing prevalence of new energy vehicles has driven a heightened demand for energy storage solutions[1–3]. Lithium-ion batteries (LIBs) have emerged as the dominant choice in the market, owing to their high capacity and extended lifespan[4,5]. Nevertheless, the constrained and uneven dispersion of lithium resources impede the sustainable progression of LIBs[6–8]. As a compelling alternative, sodium-ion batteries (SIBs) are gaining attention, leveraging their natural abundance, cost-effectiveness, safety, and reliable performance [9,10]. Unfortunately, the larger ionic radius of Na^+ (0.95 Å) compared to Li^+ (0.76 Å) leads to slower Na^+ diffusion kinetics and significant volume variation of the anode material, posing a substantial obstacle to widespread commercialization of SIBs[11–13]. Therefore, developing high-performing anodes with a practical structure and a straightforward preparation process is essential for facilitating the widespread adoption of SIBs[14,15].

Anode materials for SIBs have undergone comprehensive research, in which specific types include: i) carbon-based and titanium-based materials utilising intercalation reaction mechanisms; ii) main group metals such as Sn, Sb and Bi based on alloy reaction mechanisms; and iii) transition metal compounds utilising conversion reaction mechanisms [16–18]. Among them, researchers prefer transition metal selenides (TMSs) due to their high theoretical capacity and abundant natural availability[19]. However, the practical applications of TMSs are constrained by their substandard electronic conductivity and substantial volume variation[20,21].

To address the aforementioned shortcomings of TMSs, researchers have typically adopted structural or molecular modification strategies [21,22]. Structural modification often involves compounding with carbon materials to create composite materials with unique structures [23,24]. This approach offers two advantages: i) the carbon material aids in preventing the agglomeration of active substances, and ii) the distinctive carbon frame structure serves to alleviate stress on the material and uphold structural stability[25,26]. For example, Jiang et al. synthesized a CoSe/G composite with reduced graphene oxide (rGO) encapsulated ZIF-67 to construct a 3D interconnected structure, possessing the excellent sodium storage performance (214.0 mA h g^{-1} for 600 cycles at 2.0 A g^{-1})[27]. Furthermore, Fan et al. fabricated a core–shell $FeSe_2$@C nanorod assembled hollow nanocube by thermally induced selenization of Prussian blue microcubes, showing an extremely long cycle life (212.0 mA h g^{-1} after 3,000 cycles at 10.0 A g^{-1})[28]. Conversely, the formation of a heterogeneous interface has been noted to induce lattice defects, thereby increasing the exposure of adsorption sites. This results in an enhanced adsorption energy for Na^+ ions, expediting the removal/embedding processes within the material.[29]. Moreover, the intrinsic electric field at the heterogeneous interface redistributes electrons, optimizes the electronic structure of metal selenides, accelerates charge transport, and addresses the inherent conductivity issues of TMSs. Based on the advantages, the construction of heterogeneous structures is recognized as an effective strategy for improving the reaction kinetics and conductivity of TMSs [30,31]. For example, Zhu et al. prepared an advanced 3D Ni_3Se_4@$CoSe_2$@C/carbon nanotubes (CNTs) composite by embedding heterostructured Ni_3Se_4@$CoSe_2$ into porous carbon/CNTs by continuous carbonization and selenization[32]. The combination of 3D carbon network structure and heterogeneous interface improves the conductivity and charge transport efficiency of the materials, and boosts the sodium storage performance (243.0 mA h g^{-1} for 600 cycles at 1.0 A g^{-1}) of Ni_3Se_4 and $CoSe_2$. Besides, Zhang et al. prepared $CoSe_2$/WSe_2@C/CNs composites with a heterogeneous structure by solution method and solid-phase selenization method, showing the excellent sodium storage performance (501.9 mA h g^{-1} for 200 cycles at 0.1 A g^{-1})[33].

In this work, ZIF-67@Co-Fe PBA@RF is synthesised by ion-exchange and resorcinol–formaldehyde (RF) coating using ZIF-67 as a template, a multihole nitrogen-doped carbon-framework-constrained ($CoSe_2$/$FeSe_2$) heterogeneous anode material ($CoSe_2$/$FeSe_2$@NC@C) are obtained by the *In situ* carbonisation and selenisation. The use of a phase-rich interface and carbon confinement strategy improves the conductivity of TMSs, enhances structural stability, reduces agglomeration deactivation, and optimises reaction kinetics. Hence, the anode of $CoSe_2$/$FeSe_2$@NC@C attains a reversible capacity of 512.6 mA h g^{-1} after 150 cycles of 0.5 A g^{-1} and an superior cycling performance of 298.2 mA h g^{-1} after 1,000 cycles of 10 A g^{-1}.

2. Experimental section

2.1. Materials

Cobalt nitrate hexahydrate ($Co(NO_3)_2{\cdot}6H_2O$, AR, Sinopharm Chemical Reagent Co., Ltd.), 2-methylimidazole (2-MIM, 98 %, Aladdin Co., Ltd.), potassium ferricyanide ($K_3FeC_6N_6$ 99.95 %, Machlin Co., Ltd.), cetyltrimethylammonium bromide (CTAB, AR, Titan Technology Co., Ltd.), resorcinol ($C_6H_6O_2$, AR, Aladdin Co., Ltd.), selenium powder (Se, AR, Sinopharm Chemical Reagent Co., Ltd), formaldehyde (HCHO, AR, Sinopharm Chemical Reagent Co., Ltd) and ammonium hydroxide ($NH_3{\cdot}H_2O$, AR, Sinopharm Chemical Reagent Co., Ltd) were used directly without any purification.

2.2. Synthesis of ZIF-67 nanocubes

ZIF-67 nanocubes were synthesized via coprecipitation at room temperature. Firstly, 1.5 g $Co(NO_3)_2{\cdot}6H_2O$ and 30 mg CTAB was added to 100 mL H_2O, and the pink Solution A was obtained after stirring well. Secondly, 18.16 g 2-MIM was dissolved in 280 mL of deionised water and stirred thoroughly to produce colourless and transparent Solution B. Finally, Solution A was quickly poured into Solution B, causing an immediate color change to purple. Continuous stirring was then carried out for 20 min. The ZIF-67 cubes were obtained by washing the products through centrifugation and subsequent drying.

2.3. Synthesis of ZIF-67/Co-Fe PBA nanocubes

ZIF-67/Co-Fe PBA nanocubes were obtained via ion exchange, utilizing ZIF-67 as a template. First, 0.2 g of ZIF-67 was dispersed ultrasonically in a solution of 100 mL ethanol to obtain Solution C. Then, a solution of 0.05 g $K_3FeC_6N_6$ was dissolved in 20 mL H_2O to obtain Solution D. Finally, Solution C was rapidly added to Solution D. After a 2-hour stirring period, ZIF-67/Co-Fe PBA nanocubes were obtained through centrifugation, following by washing and drying.

2.4. Synthesis of ZIF-67/Co-Fe PBA@RF nanocubes

ZIF-67/Co-Fe PBA underwent room-temperature coating using phenolic resin as a nitrogen-doped carbon source. First, 0.4 g of ZIF-67/Co-Fe PBA was added to 40 mL of a mixed solution of H_2O and ethanol at a ratio of 7:3. After stirring for 30 min, 0.2 mL of $NH_3{\cdot}H_2O$, 0.46 g of CTAB, and 0.07 g of $C_6H_6O_2$ were added. After stirred for another 30

min, 0.12 mL of HCHO was added and stirred continuously for 8 h. Finally, ZIF-67/Co-Fe PBA@RF nanocubes were obtained through centrifugation, following by washing and drying.

2.5. Synthesis of $CoSe_2/FeSe_2$@NC@C, $CoSe_2/FeSe_2$@NC and $CoSe_2$@NC

$CoSe_2/FeSe_2$@NC@C, $CoSe_2/FeSe_2$@NC and $CoSe_2$@NC were synthesized through high-temperature pyrolysis. 0.2 g of ZIF-67/Co-Fe PBA@RF was placed at the centre of the boat, with an additional 0.15 g of Se powder at each end of the boat in a 1:1 ratio. Subsequently, the boat was placed at the centre of the tube furnace. The temperature was set to 450 °C (2 °C/min) for 2 h under a nitrogen atmosphere, and subsequently increased to 550 °C (5 °C/min) for another 2 h. The powders were then collected after cooling to obtain $CoSe_2/FeSe_2$@NC@C. On the other hand, ZIF-67/Co-Fe PBA@RF was replaced by ZIF-67/Co-Fe PBA and ZIF-67, respectively, to obtain $CoSe_2/FeSe_2$@NC and $CoSe_2$@NC with the same pyrolysis conditions.

2.6. Material characterizations

The synthetic phase structure was analyzed through powder X-ray diffraction (XRD). Raman spectroscopy (Renishaw RM 2000, UK, 514 nm laser, 5 mW power) was employed to measure the Raman spectrum. The elemental bonding was characterised using X-ray photoelectron spectroscopy (XPS, PHI 5000). Energy dispersive spectroscopy (EDS) was conducted using a field emission transmission electron microscope (TEM, Zeiss/sigma 500) equipped with an energy dispersive spectroscopy (EDS) detector. The pore characteristics and specific surface area of the samples were determined through multipoint Brunauer-Emmett-Teller (BET, ASAP2020HD8) analysis based on N_2 adsorption–desorption isotherms. The presence of vacancies in the material was assessed using electron paramagnetic resonance (EPR, Bruck-E 500).

2.7. Electrochemical measurements

The anode electrode was fabricated by uniformly coating the copper foil surface with a mixture of the active substance acetylene black (Super P) and polyvinylidene difluoride (PVDF) in *N*-methyl pyrrolidone (NMP) at a mass ratio of 7:2:1. The prepared electrodes had a loading mass of approximately 1.5 mg, with the active substance mass estimated at around 1.05 mg based on the composition of the electrode. The battery, comprising a sodium metal counterelectrode, copper foil collector, glass fiber membrane separator, and 1 M NaF_3SO_3 electrolyte dissolved in diethylene glycol dimethyl ether (DEGDME), was assembled in an argon-filled glovebox. Galvanostatic cycle tests were conducted at room temperature using a multichannel battery tester (LAND, CT 2100A, China) within a voltage window of 0.1 V to 3.0 V. The electrochemical workstation (CHI 660E, Shanghai, China) was used for electrochemical impedance spectroscopy (EIS) and cyclic voltammetry (CV) testing.

3. Results and discussion

Fig. 1 illustrates the step-by-step process for creating $CoSe_2/FeSe_2$@NC@C. First, ZIF-67 nanocubes with a length of ~ 300 nm are prepared through coprecipitation at room temperature. ZIF-67 is subjected to an ion-exchange process with $K_3[Fe(CN)_6]$ in an ethanol solvent, resulting in the production of the ZIF-67/Co-Fe PBA. Subsequently, the ZIF-67/Co-Fe PBA is coated with carbon using the room-temperature coating method, in which RF serves as the source of carbon. Finally, $CoSe_2/FeSe_2$@NC@C nanocubes of active substances ($CoSe_2/FeSe_2$) confined within a nitrogen-doped carbon framework are synthesized through selenization and in-situ carbonization.

Fig. 2 shows the surface morphology and internal structure of ZIF-67, ZIF-67/Co-Fe PBA, ZIF-67/Co-Fe PBA@RF, and $CoSe_2/FeSe_2$@NC@C. From Fig. 2**a**, the ZIF-67 presents a uniform cubic structure with a length of ~ 300 nm. The ZIF-67/Co-Fe PBA is derived from ZIF-67 by ion exchange. As shown in Fig. 2**b**, the ZIF-67/Co-Fe PBA features a double-layer structure, enclosing ZIF-67 within Co-Fe PBA. However, the bilayer structure is prone to collapse during carbonization, so the ZIF-67/Co-Fe PBA is coated with RF for structural stabilization. From Fig. 2**c**, the morphology of the ZIF-67/Co-Fe PBA@RF is similar to that of the ZIF-67, both of which are cubic structures, but the surface of the ZIF-67/Co-Fe PBA@RF is rougher. As shown in Fig. 2**d**, the $CoSe_2/FeSe_2$@NC@C retains a cubic structure after selenization and carbonization, which is attributed to the formation of a rigid carbon framework around the material after carbonization. On the contrary, $CoSe_2$@NC and $CoSe_2/FeSe_2$@NC in **Figs. S1(a,b)** exhibit severe collapse and agglomeration after selenization and carbonization. Furthermore, the TEM technique is utilized to investigate the internal structure and morphology of the $CoSe_2/FeSe_2$@NC composite. As shown in Fig. 2**(e, f)** and Fig. S1**c**, the $CoSe_2/FeSe_2$@NC@C is cuboidal and uniformly distributed. From Fig. 2**f**, the RF-derived carbon skeleton of the $CoSe_2/FeSe_2$@NC@C can be visually observed with a thickness of 40 – 50 nm. The carbon framework effectively prevents the material from collapsing and pulverizing during the cycle, protecting the internal active material [34,35]. In the HRTEM images (Fig. 2**g** and Fig. 2**h**) of the $CoSe_2/FeSe_2$@NC@C, the (1 0 1) and (1 2 0) planes of $FeSe_2$ and (1 2 0) and (1 1 1) planes of $CoSe_2$ are clearly visible with lattices of 0.287, 0.248, 0.249 and 0.261 nm, respectively. In addition, it is evident from Fig. 2**(g, h)** that $CoSe_2/FeSe_2$ exhibits a rich heterogeneous interface, as evidenced by the distinct phase boundary delineated by red lines. It is noteworthy that the abundant phase interface generates numerous inherent electric fields, thereby expediting electron transport and augmenting the intrinsic conductivity of the TMSs[36]. In addition, the SAED pattern of the $CoSe_2/FeSe_2$@NC@C is presented in Fig. 2**i**, where the yellow ring corresponds to the (2 1 0), (1 2 0) and (1 0 1) lattice planes of the $FeSe_2$, and the white ring corresponds to the (1 0 1) and (1 1 1) lattice planes of $CoSe_2$, which further demonstrates the successful preparation of the $CoSe_2/FeSe_2$. Fig. 2**j** illustrates the uniform distribution of Co, Fe, C, N, Se, and other elements in the composite, which confirms the successful synthesis of the $CoSe_2/FeSe_2$@NC@C composite. Furthermore, the

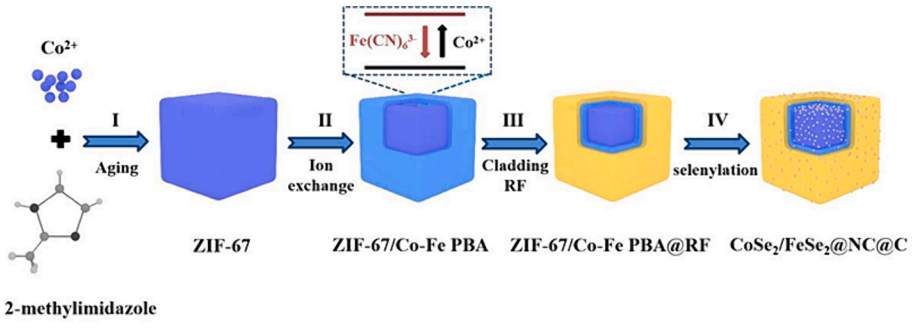

Fig. 1. Synthesis steps of $CoSe_2/FeSe_2$@NC@C.

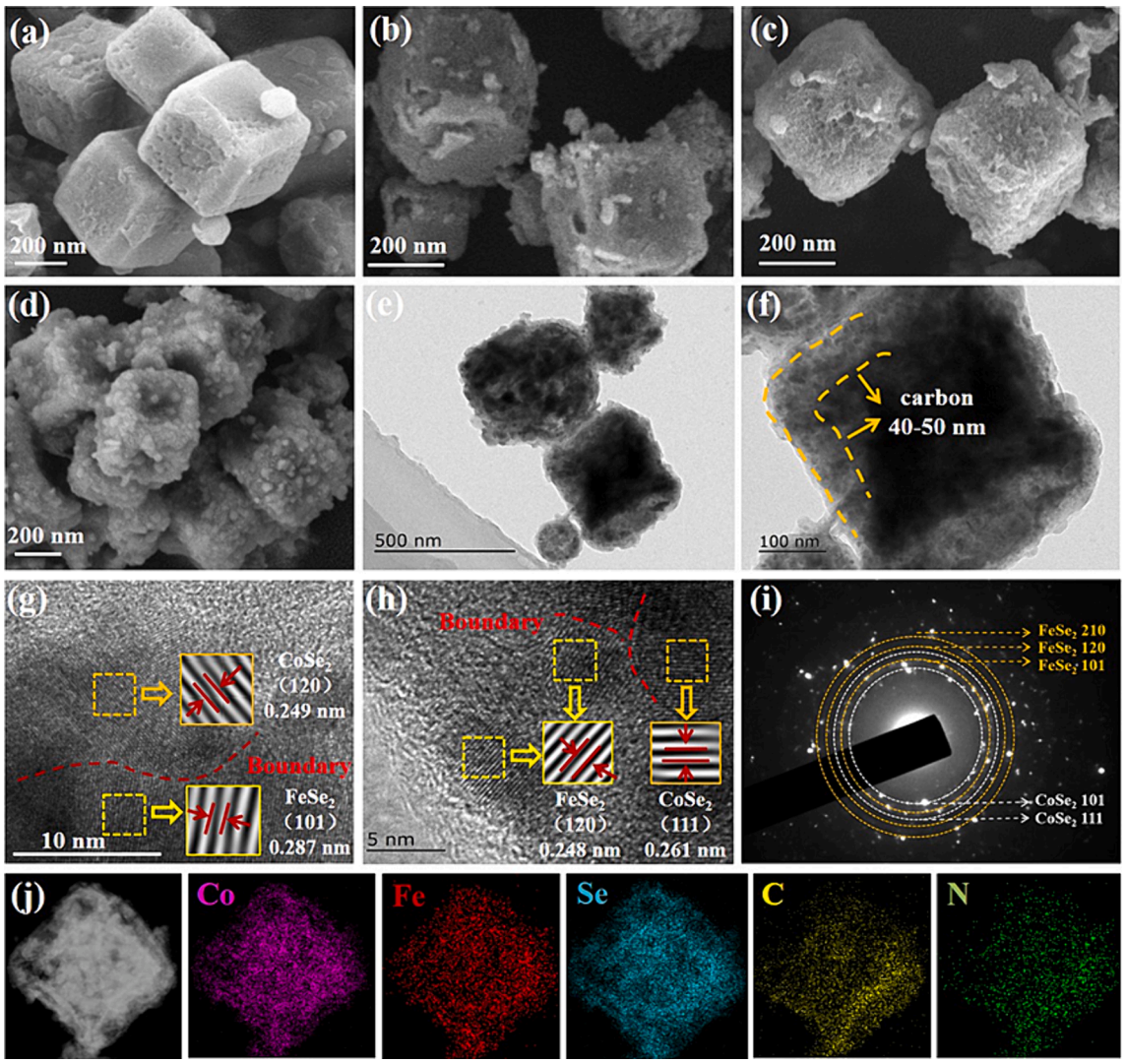

Fig. 2. (a) SEM image of ZIF-67; (b) SEM image of ZIF-67/Co-Fe PBA; (c) SEM image of ZIF-67/Co-Fe PBA@RF; (d) SEM image of $CoSe_2/FeSe_2$@NC@C; (e-f) TEM images of $CoSe_2/FeSe_2$@NC@C; (g-h) HRTEM image of $CoSe_2/FeSe_2$@NC@C; (i) SAED pattern of $CoSe_2/FeSe_2$@NC@C; (j) TEM EDS elemental images of $CoSe_2/FeSe_2$@NC@C.

elemental content (as shown in Fig. S2) of $CoSe_2/FeSe_2$@NC@C has been examined using EDS to ensure precision and accuracy.

Fig. 3**a** and Figs. S3**(a, b)** show the XRD spectra of $CoSe_2/FeSe_2$@NC@C, $CoSe_2/FeSe_2$@NC and $CoSe_2$@NC, respectively, to verify the successful synthesis of substances. As shown in Fig. 3**a** and Fig. S2**a**, the diffraction peaks in the spectra correspond precisely to the cubic-phases $CoSe_2$(JCPDS # 53–0449) and $FeSe_2$(JCPDS # 21–0432) without spurious peaks. From Fig. S2**b**, the diffraction peak in the pattern corresponds exactly to the cubic phase $CoSe_2$ (JCPDS # 53–0449). It is proved that $CoSe_2/FeSe_2$@NC@C, $CoSe_2/FeSe_2$@NC and $CoSe_2$@NC composites exhibit high purity. In addition, the Raman spectra, as shown in Fig. 3**b**, reveal two distinct broad peaks at 1339 and 1588 cm^{-1}, corresponding to sp^3-hybrid disorder (D) and sp^2-hybrid graphene (G), respectively. In composite materials, a reduced ratio of the D-band and G-band indicates an elevated level of carbon graphitization, leading to the improvement of conductivity. The results show that the $CoSe_2/FeSe_2$@NC@C (I_D/I_G = 0.83) has higher conductivity than the $CoSe_2/FeSe_2$@NC (I_D/I_G = 0.85) and $CoSe_2$@NC (I_D/I_G = 0.86). To validate the structural advantages of $CoSe_2/FeSe_2$@NC@C, the precise surface area and pore size distribution of the three components are examined. Fig. 3**c** illustrates that the pore sizes of $CoSe_2/FeSe_2$@NC@C, $CoSe_2/FeSe_2$@NC and $CoSe_2$@NC composites are primarily mesoporous. Moreover, the pore volume of $CoSe_2/FeSe_2$@NC@C is greater than those of $CoSe_2/FeSe_2$@NC and $CoSe_2$@NC. Additionally, Fig. 3**d** demonstrates that the specific surface area of the $CoSe_2/FeSe_2$@NC@C (69.52 $m^2\ g^{-1}$) composite is superior to those of $CoSe_2/FeSe_2$@NC (43.46 $m^2\ g^{-1}$) and $CoSe_2$@NC (22.69 $m^2\ g^{-1}$). The $CoSe_2/FeSe_2$@NC@C material possesses an increased specific surface area and mesoporous pore capacity, facilitating complete electrolyte infiltration and exposing more reactive sites, enhancing the reaction kinetics of the material[31,37].

The composition and valence states of elements in the $CoSe_2/FeSe_2$@NC@C, $CoSe_2/FeSe_2$@NC and $CoSe_2$@NC composites are investigated by XPS. As illustrated on Fig. S4, the $CoSe_2/FeSe_2$@NC@C and $CoSe_2/FeSe_2$@NC composites comprised of Co, N, C, Se, Fe, and O, while the CoSe2@NC composite contained Co, N, C, Se, and O elements. The oxygen elements present in the sample are due to the oxidising reaction which occurred during the assay. The diagram in Fig. 3**e** illustrates that the two auxiliary peaks of the $CoSe_2/FeSe_2$@NC@C, $CoSe_2/FeSe_2$@NC and $CoSe_2$@NC are represented by 787.1 eV/803.2 eV, 787.2 eV/803.3 eV and 786.7 eV/802.5 eV, respectively, in the Co 2p spectra. The two Co^{2+} $2p_{1/2}$ spin orbits within $CoSe_2/FeSe_2$@NC@C, $CoSe_2/FeSe_2$@NC and $CoSe_2$@NC are situated at 782.7 eV/798.8 eV, 782.8 eV/798.8 eV and 782.0 eV/797.9 eV, respectively. In addition, the two Co^{3+} $2p_{3/2}$

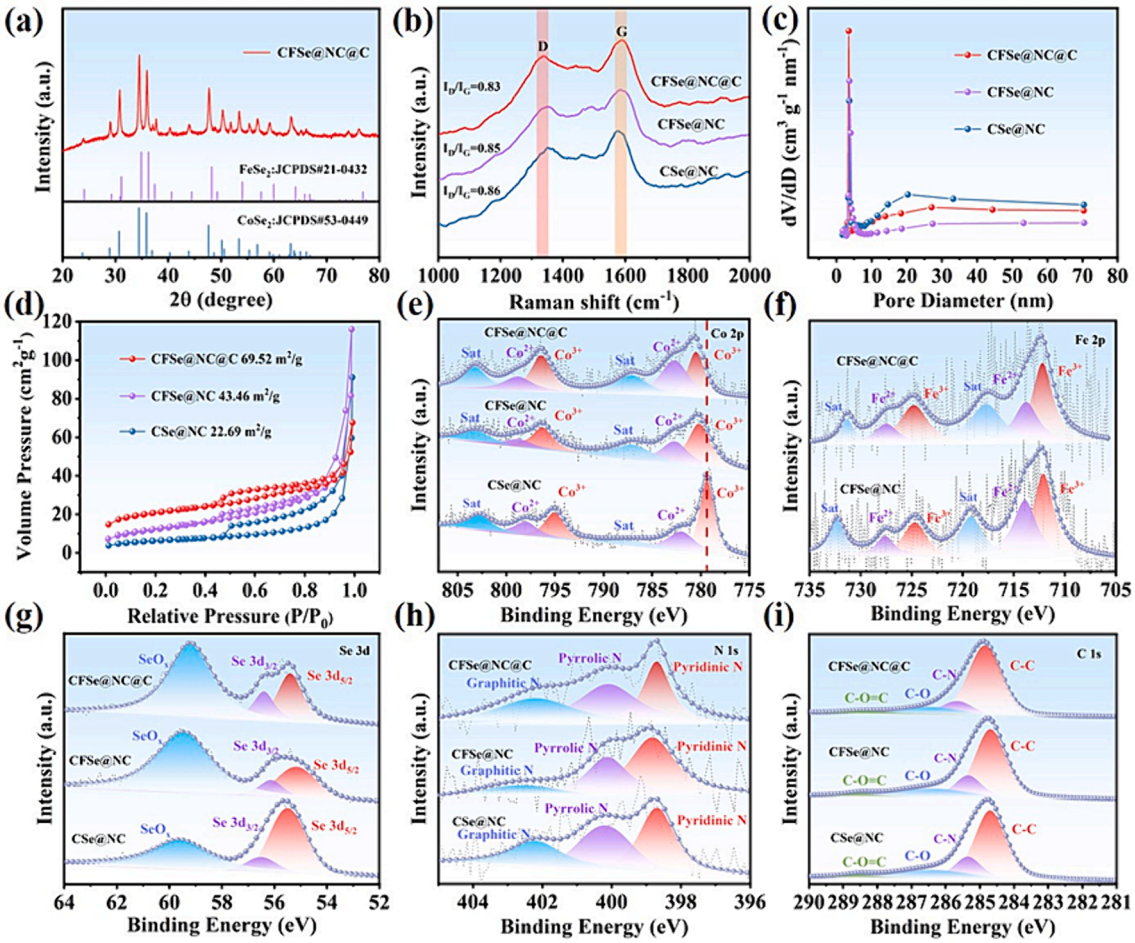

Fig. 3. (a) XRD pattern of $CoSe_2/FeSe_2$@NC@C; (b) Raman spectra of $CoSe_2/FeSe_2$@NC@C, $CoSe_2/FeSe_2$@NC and $CoSe_2$@NC; (c) Pore size distribution of $CoSe_2/FeSe_2$@NC@C, $CoSe_2/FeSe_2$@NC and $CoSe_2$@NC; (d) N_2 adsorption–desorption isotherms of $CoSe_2/FeSe_2$@NC@C, $CoSe_2/FeSe_2$@NC and $CoSe_2$@NC; (e) XPS spectra of Co 2p of $CoSe_2/FeSe_2$@NC@C, $CoSe_2/FeSe_2$@NC and $CoSe_2$@NC; (f) XPS spectra of Fe 2p of $CoSe_2/FeSe_2$@NC@C, $CoSe_2/FeSe_2$@NC; (g-i) XPS spectra of Se 3d, C 1 s and N1s of $CoSe_2/FeSe_2$@NC@C, $CoSe_2/FeSe_2$@NC and $CoSe_2$@NC.

spin orbits within $CoSe_2/FeSe_2$@NC@C, $CoSe_2/FeSe_2$@NC and $CoSe_2$@NC are located at 780.4 eV/796.4 eV, 780.3 eV/796.4 eV, and 779.4 eV/795.0 eV, respectively. It should be noted that the Co^{2+} $2p_{1/2}$ and Co^{3+} $2p_{3/2}$ peaks of the $CoSe_2/FeSe_2$@NC@C and $CoSe_2/FeSe_2$@NC exhibit a positive shift compared to $CoSe_2$@NC. This shift is a result of electron transfer from $CoSe_2$ to $FeSe_2$, which is driven by the built-in electric field of the heterogeneous interface[31,38]. This finding demonstrates a robust electronic interaction within the $CoSe_2$ and $FeSe_2$ interface, resulting in the redistribution of charges between $CoSe_2$ and $FeSe_2$[38]. Consequently, the optimized electronic structure of the $CoSe_2/FeSe_2$@NC@C improves the intrinsic conductivity [38,39]. As illustrated in Fig. 3**f**, the Fe 2p spectra of the $CoSe_2/FeSe_2$@NC@C and $CoSe_2/FeSe_2$@NC show two satellite peaks located at 717.6 eV/731.3 eV and 719.2 eV/732.2 eV, respectively. The $CoSe_2/FeSe_2$@NC@C and $CoSe_2/FeSe_2$@NC exhibit two peaks at 712.2 eV/724.8 eV and 712.1 eV/724.7 eV, respectively, in the Fe^{3+} $2p_{3/2}$ spectra, as well as two peaks at 713.8 eV/727.5 eV and 713.9 eV/727.6 eV, respectively, in the Fe^{2+} $2p_{1/2}$ spectra. The positions of the $3d_{5/2}$, $3d_{3/2}$ and SeO_x peaks in the Se 3d spectra of $CoSe_2/FeSe_2$@NC@C, $CoSe_2/FeSe_2$@NC and $CoSe_2$@NC are represented by 55.2 eV/55.1 eV/55.5 eV, 56.2 eV/55.9 eV/56.5 eV and 59.2 eV/58.9 eV/59.6 eV respectively, as indicated in Fig. 3**g**. The Se 3d peaks of $CoSe_2/FeSe_2$@NC@C and $CoSe_2/FeSe_2$@NC exhibit varying degrees of negative offset when compared to $CoSe_2$@NC. This difference may be attributed to the notable presence of Se vacancies (**Fig. S5**) at the rich heterogeneous interface, weakening the interaction between selenium and iron atoms[29,40]. In Fig. 3**h**, the peak positions of pyridine-N, pyrrole-N and graphene-N of N elements of $CoSe_2/FeSe_2$@NC@C, $CoSe_2/FeSe_2$@NC and $CoSe_2$@NC are 398.7 eV/398.8 eV/398.7 eV, 400.1 eV/400.2 eV/400.1 eV and 402.2 eV/402.4 eV/402.2 eV, respectively. In addition, Fig. 3**i** shows that the four C—C, C—N, C—O, C-O=C bands of $CoSe_2/FeSe_2$@NC@C, $CoSe_2/FeSe_2$@NC and $CoSe_2$@NC are located at 284.8 eV/284.7 eV/284.7 eV, 285.6 eV/285.3 eV/285.3 eV, 286.4 eV/286.4 eV/286.3 eV, 288.4 eV/288.4 eV/288.4 eV, respectively. The presence of the C—N peak confirms the successful nitrogen doping of the carbon layer, leading to improved conductivity and reaction kinetics[41].

To demonstrate the advantageous features of $CoSe_2/FeSe_2$@NC@C in sodium storage, we assembled a 2032 coin-type cell with $CoSe_2/FeSe_2$@NC@C as the anode and proceeded to evaluate its electrochemical properties. Fig. 4**a** records the first five CV curves at the scan rate of 0.1 mV s^{-1}. In the first cathodic scan, a sharp and strong peak at ~ 1.0 eV corresponds to the first insertion of Na^+ into the anode material and the formation of a solid electrolyte interface (SEI)[42,43]. It is worth mentioning that the above strong peak disappears in the subsequent cathodic scan, indicating that the formation of SEI is an irreversible process, which can also elucidate the reason behind the initial loss of capacity of SIBs in the first cycle. In the following anodic scan, a small peak and a broad peak appear at 1.5 eV and 1.85 eV, respectively, indicating that Fe and Co metals and Na_2Se are reversed to form $FeSe_2$ and $CoSe_2$ again. During the second cathodic scan, a reaction occurs where Na^+ is embedded at 1.5 eV, and Fe^0 and Co^0 were generated at 0.72 eV. In addition, the curves of the subsequent CV scans almost

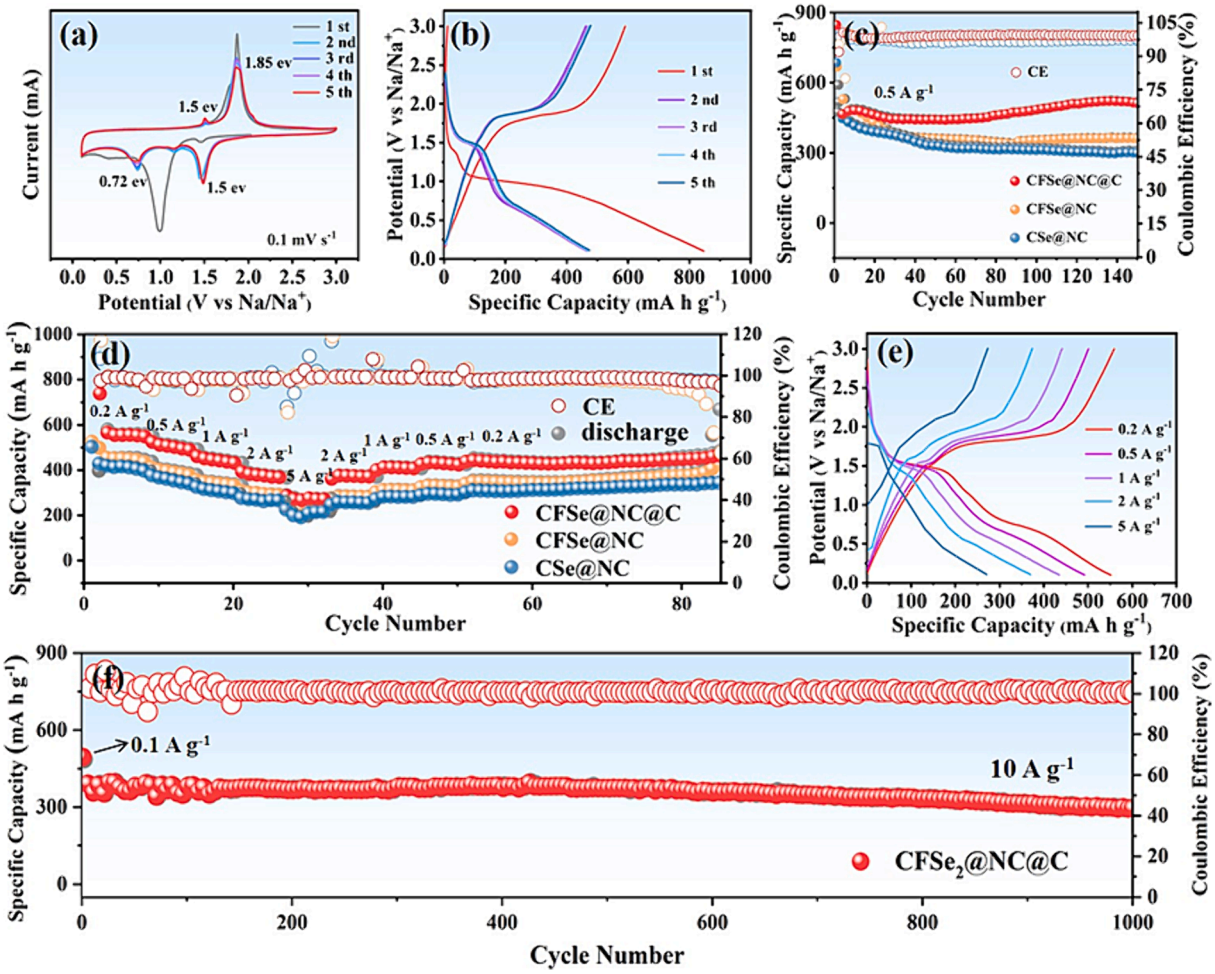

Fig. 4. (a) CV tests of $CoSe_2/FeSe_2$@NC@C electrode; (b) Discharge-charge cycle curves at 0.5 A g^{-1}; (c) Cycling stability of $CoSe_2/FeSe_2$@NC@C, $CoSe_2/FeSe_2$@NC and $CoSe_2$@NC cathodes at 0.5 A g^{-1}; (d) Rate performance of $CoSe_2/FeSe_2$@NC@C, $CoSe_2/FeSe_2$@NC and $CoSe_2$@NC; (e) Discharge-charge cycle curves at various current densities; (f) Long-term cyclic stability of $CoSe_2/FeSe_2$@NC@C at 10 A g^{-1}.

overlap, indicating that the $CoSe_2/FeSe_2$@NC@C composite has superb reversibility. From Fig. 4**b**, the charge and discharge specific capacities of $CoSe_2/FeSe_2$@NC are 842.8 mA h g^{-1} and 591.6 mA h g^{-1} at 0.5 A g^{-1}, respectively, and the first round Coulomb efficiency is 70.2 %. In addition, the Coulomb efficiency is almost 100 % and the reversible capacity gradually rises in the following cycles. From Fig. 4**c**, the $CoSe_2/FeSe_2$@NC@C electrode provides a reversible capacity of 512.6 mA h g^{-1} at 0.5 A g^{-1} after 150 cycles. It is important to highlight that the capacity of the CoSe2/FeSe2@NC@C electrode exhibits a tendency to decrease after the first cycle. This phenomenon is attributed to the continuous formation of a SEI on the material surface during the initial cycle, where Na^+ and anions from the electrolyte contribute to the SEI formation. Some of the Na^+ is consumed in this process, resulting in an irreversible capacity loss[44,45]. Additionally, the formation of the SEI film and the carbon layer coated on the electrode surface hinders the full penetration of electrolyte molecules inside the active material, resulting in a gradual decrease in capacity in subsequent cycles[46–48]. As the SEI stabilises, Na^+ diffusion kinetics improve, and the sodiation-induced reactivation contributes to a gradual rise in capacity[49]. In contrast, $CoSe_2/FeSe_2$@NC and $CoSe_2$@NC exhibit poor reversible capacities of 361.1 mA h g^{-1} and 302.2 mA h g^{-1} at 0.5 A g^{-1}, respectively. Similarly, $CoSe_2/FeSe_2$@NC@C shows the better rate performance than $CoSe_2/FeSe_2$@NC and $CoSe_2$@NC (Fig. 4**d**), delivering the reversible capacities of 547.1, 488.4, 430.5, 366.8 and 274.6 mA h g^{-1} at 0.2, 0.5, 1.0, 2.0 and 5.0 A g^{-1}, respectively. The reversible capacities of the $CoSe_2/FeSe_2$@NC@C can be maintained at 471.6 mA h g^{-1} by restoring 5.0 A g^{-1} to 0.2 A g^{-1}, even after undergoing 35 cycles at 0.2 A g^{-1}. From Fig. 4**e, a** clear charge–discharge plateau can be observed at different current densities, indicating that the $CoSe_2/FeSe_2$@NC@C composite is weakly polarized. To further demonstrate the cyclic stability of the $CoSe_2/FeSe_2$@NC@C composite, the cell was tested at a high current density (Fig. 4**f**). The reversible capacity of 298.2 mA h g^{-1} is still retained at 10 A g^{-1} after 1,000 cycles, and the capacity retention rate is as high as 75.3 %. The reversible capacity and cyclic stability of $CoSe_2/FeSe_2$@NC@C are comparable to, or even surpass, those presented in the reported work on selenide anodes as listed in **Table S1**. The superior cycling stability of $CoSe_2/FeSe_2$@NC@C primarily stems from the protective effect provided by the rigid carbon skeleton and *N*-doped carbon matrix on the active materials. Additionally, the heterogeneous interfacial effect of $CoSe_2/FeSe_2$ plays a crucial role, inhibiting material deactivation through agglomeration and enhancing the intrinsic conductivity of the material[31,37].

Fig. 5**a** shows the CV curves of $CoSe_2/FeSe_2$@NC@C at various sweeping speeds for an analysis of reaction kinetics. As the scanning rate increases from 0.2 to 1.0 mV s^{-1}, the peaks in the CV curves almost coincide, suggesting excellent cycle reversibility of the $CoSe_2/FeSe_2$@NC@C electrode. In general, the theoretical relationship between scan rate (v) and peak current (i) of CV curves can be derived from the following formulas[14,50]:

$$i_1 = av^b \quad (1)$$

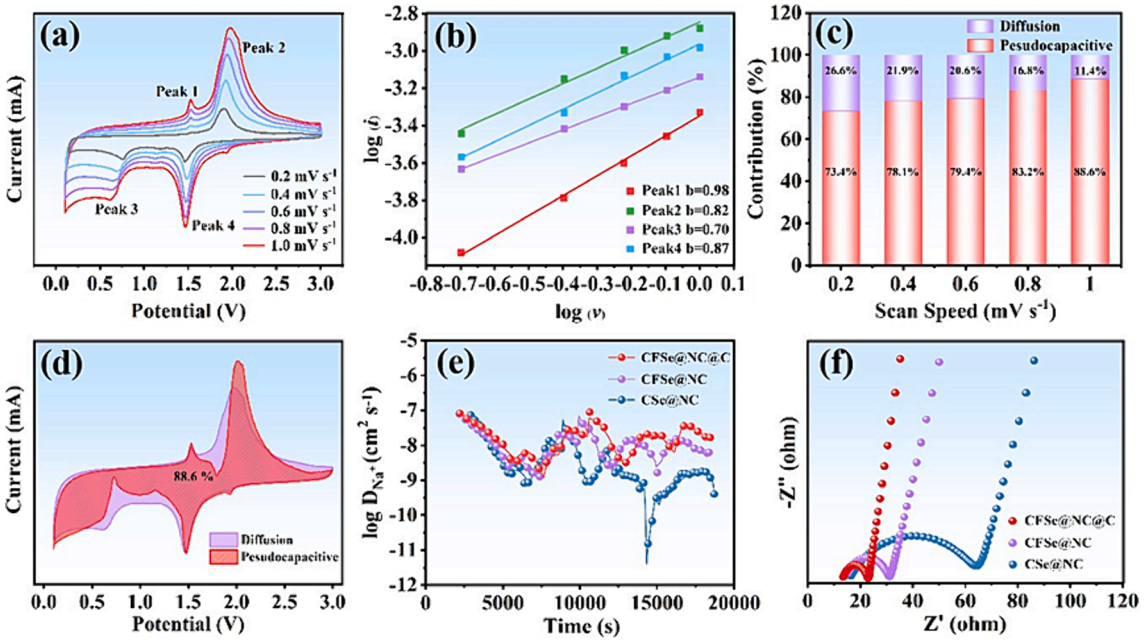

Fig. 5. (a) CV curves of $CoSe_2/FeSe_2$@NC@C at different scan rates from 0.2 to 1.0 mV s^{-1}; (b) Fitting lines of log *v* (scan rate)-log *i* (peak current) for $CoSe_2/FeSe_2$@NC@C; (c) Bar chart of contribution rate of pseudocapacitive for $CoSe_2/FeSe_2$@NC@C electrodes; (d) Capacitance contribution (red area) rate of $CoSe_2/FeSe_2$@NC@C at 1.0 mV s^{-1}; (e) Calculated log(D_{Na+}) of $CoSe_2/FeSe_2$@NC@C, $CoSe_2/FeSe_2$@NC and $CoSe_2$@NC anodes; (f) Nyquist plots of $CoSe_2/FeSe_2$@NC@C, $CoSe_2/FeSe_2$@NC and $CoSe_2$@NC anodes.

$$log(i_1) = blog(v) + log(a) \quad (2)$$

Based on prior research, the general sodium storage is regulated by both pseudo-capacitance contribution and ion diffusion contribution [51,52]. When the b-value closes to 1, the sodium storage is mainly controlled by the pseudo-capacitance behavior. When the b-value closes to 0.5, the storage is mainly regulated by the ion diffusion behavior. As shown in Fig. 5**b**, the fitting b-values of anodic peak are 0.98 and 0.82, respectively, while the fitting b-values of cathodic peak are 0.70 and 0.87, respectively. These values suggest that the sodium storage mechanism of the $CoSe_2/FeSe_2$@NC@C electrode is primarily regulated by pseudo-capacitance. In addition, the specific contribution proportion of the pseudo-capacitance contribution can be calculated by Equation (3) [53]:

$$i = k_1 v + k_2 v^{1/2} \quad (3)$$

As demonstrated in Fig. 5**(c, d)**, when the CV scanning rate is 0.2 – 1.0 mV s^{-1}, the contribution proportions of pseudo-capacitance behavior are 73.4 %, 78.1 %, 79.4 %, 83.2 % and 88.6 %, respectively. The high pseudo-capacitance contribution rate of the $CoSe_2/FeSe_2$@NC@C composite is attributed to the existence of a large number of heterogeneous interfaces, and the electric field existing at the heterogeneous interface accelerates the charge transport and optimizes the Na^+ adsorption, thereby enhancing the reaction kinetics of the material. To investigate the factors influencing high-rate sodium storage of $CoSe_2/FeSe_2$@NC and $CoSe_2$@NC, we have conducted CV tests at various sweep rates for the samples. Fig. S6**a and S7a** illustrate that the peaks of the CV curves for $CoSe_2/FeSe_2$@NC and $CoSe_2$@NC nearly coincide as the scan rate increases from 0.2 mV s^{-1} to 1.0 mV s^{-1}, indicating good cycle reversibility. Furthermore, in Fig. S6**b and S7b**, it can be observed that as the CV scanning rate ranges from 0.2 mV s^{-1} to 1.0 mV s^{-1}, the pseudo-capacitance behavior of the $CoSe_2/FeSe_2$@NC accounts for 67 %, 74 %, 78 %, 80 %, and 82 %, respectively, while that of the $CoSe_2$@NC accounts for 60 %, 66 %, 70 %, 72 % and 78 %, respectively. In summary, the high sodium storage behavior of $CoSe_2/FeSe_2$@NC and $CoSe_2$@NC is also attributed to pseudo-capacitance.

In order to further verify the advantage of the heterogeneous structure on the reaction kinetics of the electrode material, the diffusion coefficient of Na^+ at 0.1 V – 3.0 V is tested by the galvanostatic intermittent titration technique (GITT). The specific value of the diffusion coefficient of Na^+ can be obtained by the following formula[43]:

$$D_{Na+} = \frac{4}{\tau\pi}\left(\frac{n_m V_m}{S}\right)^2\left(\frac{\Delta E_s}{\Delta E_t}\right)^2 \quad (4)$$

As shown in Fig. 5**e**, the diffusion coefficients of Na^+ in the $CoSe_2/FeSe_2$@NC and $CoSe_2/FeSe_2$@NC electrodes is smaller than that in the $CoSe_2$@NC electrode, indicating that the $CoSe_2/FeSe_2$ heterostructure can indeed promote the rapid migration of Na^+ in the electrode material. Moreover, the conductivity of $CoSe_2/FeSe_2$@NC@C, $CoSe_2/FeSe_2$@NC and $CoSe_2$@NC electrodes is tested. The impedance value of the $CoSe_2/FeSe_2$@NC@C electrode (9.5 Ω) is smaller compared to that of $CoSe_2/FeSe_2$@NC (17.2 Ω) and $CoSe_2$@NC (51.7 Ω), as shown in Fig. 5**f** through equivalent circuit analysis (**Fig. S8**). The results indicate that the presence of heterogeneous interface and RF-derived carbon framework promotes electron transport and enhances the intrinsic conductivity of $CoSe_2/FeSe_2$@NC@C composite.

Furthermore, in the investigation of the sodium storage mechanism of the $CoSe_2/FeSe_2$@NC@C, the material transformation of $CoSe_2/FeSe_2$ nanoparticles is observed in the *in situ* XRD method during the first charging and discharging cycle from an open-circuit voltage (OCV) to 3.0 V at 0.5 A g^{-1} as shown in Fig. 6**a**. To clearly show the material changes of $CoSe_2/FeSe_2$ nanoparticles during charging and discharging, the *in situ* XRD spectra are converted into contour plots (Fig. 6**b**). The colours distinguish between various diffraction peaks, with increasing intensity displayed as the colour shifts from blue to pink. As shown in Fig. 6**b**, the clear diffraction peaks at 30.7°, 34.4°, 35.8° and 47.6° are visible in the initial XRD contour plots, corresponding to the (101), (111), (120) and (211) crystal planes of the $CoSe_2$, respectively, while the diffraction peaks at 34.4° and 35.8° correspond to the (111) and (120) crystal faces, respectively, of the $FeSe_2$. As the potential drops to ~ 1.0 V, the diffraction peaks of $CoSe_2$ and $FeSe_2$ gradually fade. Conversely, the peaks of the (111) and (220) crystal faces of $NaSe_2$ (PDF No.74–1161) and the (110) crystal planes of Co (PDF No.15–0806)

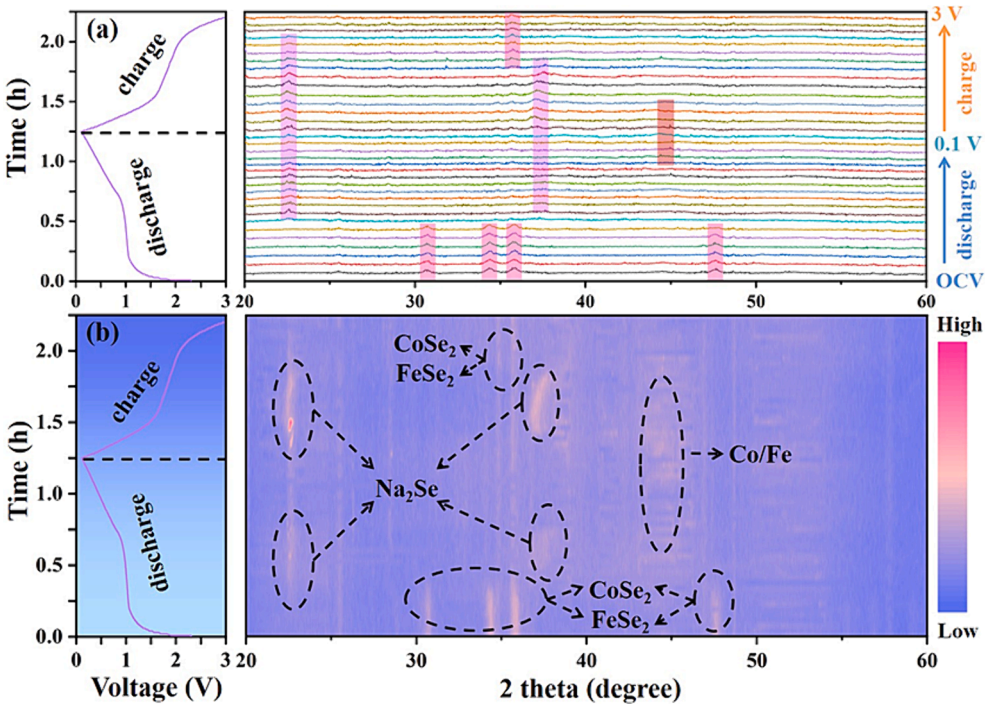

Fig. 6. (a) *In situ* XRD patterns and (b) contour plots of $CoSe_2$/$FeSe_2$ undergoing discharge/charge cycles from the OCV to 3.0 V.

and Fe (PDF No.06–0696) begin to form steadily, indicating the conversion reaction of Na^+ with $CoSe_2$ and $FeSe_2$[54,55]. In addition, the intensity of diffraction peaks for $NaSe_2$, Co and Fe gradually decreases with the increasing charging voltage, and the appearance of (1 1 1) and (1 2 0) crystal planes for $CoSe_2$ and $FeSe_2$ indicates a reverse conversion reaction of $NaSe_2$, Co and Fe[55,56]. It is noteworthy that the magnitude of the last appearing signals of $CoSe_2$ and $FeSe_2$ is low, which is attributed to the poor crystallization of the re-formed $CoSe_2$ and $FeSe_2$. The reappearance of $CoSe_2$ and $FeSe_2$ demonstrates the excellent cycle reversibility of the $CoSe_2$/$FeSe_2$@NC@C composite. The specific sodium storage reaction mechanisms of $CoSe_2$/$FeSe_2$@NC@C are as follows [38,57,58]:

$$CoSe2 + xNa+ \leftrightarrow NaxCoSe2 \quad (5)$$

$$FeSe2 + xNa+ \leftrightarrow NaxFeSe2 \quad (6)$$

$$NaxCoSe2+(4-x)Na+ \leftrightarrow Co0 + 2Na2Se \quad (7)$$

$$NaxFeSe2+(4-x)Na+ \leftrightarrow Fe0 + 2Na2Se \quad (8)$$

4. Conclusion

In conclusion, we have built a spatially carbon-constrained $CoSe_2$/$FeSe_2$@NC@C nanocubic composite with rich heterogeneous interfaces through ion exchange and carbon confinement strategies. The *N*-enriched carbon matrix and RF-derived carbon backbone effectively inhibit agglomerate deactivation, relieve internal tension, maintain structural integrity and ultimately provide superior durability[42]. The numerous heterogeneous interfaces reveal numerous active sites, thus enhancing the absorption energy of Na^+ and the overall storage utility of sodium within the material[59]. Additionally, the embedded electric field at the heterogeneous interfaces leads to electron redistribution, resulting in the improvement of the electronic structure and intrinsic conductivity of the material[60]. Therefore, the $CoSe_2$/$FeSe_2$@NC@C exhibits exceptional cycling performance, with reversible capacities of 512.6 mA h g^{-1} after 150 cycles at 0.5 A g^{-1}, and 298.2 mA h g^{-1} after 1,000 cycles at 10 A g^{-1}. In this study, we propose a novel method for preparing promising anodes for SIBs through the strategies of carbon confinement and heterogeneous interfaces. This innovative approach deserves further exploration and consideration in the field [60,61].

CRediT authorship contribution statement

Peng Wang: Writing – original draft, Software, Methodology, Investigation, Conceptualization. **Xiangyue Liao:** Visualization, Software, Formal analysis. **Min Xie:** Visualization, Data curation. **Qiaoji Zheng:** Software, Formal analysis. **Yuxiang Chen:** Software, Formal analysis. **Kwok-Ho Lam:** Writing – review & editing, Validation, Resources. **Heng Zhang:** Methodology, Investigation. **Dunmin Lin:** Writing – review & editing, Resources, Funding acquisition.

Declaration of competing interest

The authors declare that they have no known competing financial interests or personal relationships that could have appeared to influence the work reported in this paper.

Data availability

Data will be made available on request.

Acknowledgements

This work was supported by Natural Science Foundation of Sichuan Province (2022NSFSC0222) and Sichuan Science and Technology Program (2023NSFSC0439) of China. The authors also appreciate the Shiyanjia Lab (www.shiyanjia.com) for the SEM tests, eceshi (www.eceshi.cn) for the EPR tests and Beijing Nordson Rongke Technology Co. LTD (www.kexingtest.com) for the XPS tests.

Appendix A. Supplementary data

Supplementary data to this article can be found online at https://doi.

org/10.1016/j.jcis.2024.03.107.

References

[1] Y.E. Durmus, H. Zhang, F. Baakes, G. Desmaizieres, H. Hayun, L. Yang, M. Kolek, V. Küpers, J. Janek, D. Mandler, Side by side battery technologies with lithium-ion based batteries, Adv. Energy Mater. 10 (24) (2020) 2000089.

[2] F. Wu, J. Maier, Y. Yu, Guidelines and trends for next-generation rechargeable lithium and lithium-ion batteries, Chem. Soc. Rev. 49 (5) (2020) 1569–1614.

[3] B. Scrosati, J. Hassoun, Y.-K. Sun, Lithium-ion batteries, A Look into the Future, Energy & Environmental Science 4 (9) (2011) 3287–3295.

[4] M. Wakihara, Recent developments in lithium ion batteries, Mater. Sci. Eng. R. Rep. 33 (4) (2001) 109–134.

[5] V. Etacheri, R. Marom, R. Elazari, G. Salitra, D. Aurbach, Challenges in the development of advanced li-ion batteries: a review, Energ. Environ. Sci. 4 (9) (2011) 3243–3262.

[6] M. Li, J. Lu, Z. Chen, K. Amine, 30 years of lithium-ion batteries, Adv. Mater. 30 (33) (2018) 1800561.

[7] X. Ma, L. Azhari, Y. Wang, Li-ion battery recycling challenges, Chem 7 (11) (2021) 2843–2847.

[8] T. Liu, J. Lu, F. Lin, Lattice strain blights lithium-ion batteries, Nature 305 (2022) 312.

[9] C. Vaalma, D. Buchholz, M. Weil, S. Passerini, A cost and resource analysis of sodium-ion batteries, Nat. Rev. Mater. 3 (4) (2018) 1–11.

[10] W. Zhang, F. Zhang, F. Ming, H.N. Alshareef, Sodium-ion battery anodes: status and future trends, EnergyChem 1 (2) (2019) 100012.

[11] D. Hou, D. Xia, E. Gabriel, J.A. Russell, K. Graff, Y. Ren, C.-J. Sun, F. Lin, Y. Liu, H. Xiong, Spatial and temporal analysis of sodium-ion batteries, ACS Energy Lett. 6 (11) (2021) 4023–4054.

[12] K. Sada, J. Darga, A. Manthiram, Challenges and prospects of sodium-ion and potassium-ion batteries for mass production, Adv. Energy Mater. (2023) 2302321.

[13] Y. Sun, S. Guo, H. Zhou, Exploration of advanced electrode materials for rechargeable sodium-ion batteries, Adv. Energy Mater. 9 (23) (2019) 1800212.

[14] J. Deng, W.B. Luo, S.L. Chou, H.K. Liu, S.X. Dou, Sodium-ion batteries: from academic research to practical commercialization, Adv. Energy Mater. 8 (4) (2018) 1701428.

[15] H. Zhang, I. Hasa, S. Passerini, Beyond insertion for na-ion batteries: nanostructured alloying and conversion anode materials, Adv. Energy Mater. 8 (17) (2018) 1702582.

[16] M. Lao, Y. Zhang, W. Luo, Q. Yan, W. Sun, S.X. Dou, Alloy-based anode materials toward advanced sodium-ion batteries, Adv. Mater. 29 (48) (2017) 1700622.

[17] Q. Gu, J.A. Kimpton, H.E. Brand, Z. Wang, S. Chou, Solving key challenges in battery research using in situ synchrotron and neutron techniques, Adv. Energy Mater. 7 (24) (2017) 1602831.

[18] L. Li, Y. Zheng, S. Zhang, J. Yang, Z. Shao, Z. Guo, Recent progress on sodium ion batteries: potential high-performance anodes, Energ. Environ. Sci. 11 (9) (2018) 2310–2340.

[19] Y. Huang, Z. Wang, M. Guan, F. Wu, R. Chen, Toward rapid-charging sodium-ion batteries using hybrid-phase molybdenum sulfide selenide-based anodes, Adv. Mater. 32 (40) (2020) 2003534.

[20] Y. Gong, Y. Li, Y. Li, M. Liu, Y. Bai, C. Wu, Metal selenides anode materials for sodium ion batteries: synthesis, modification, and application, Small 19 (4) (2023) 2206194.

[21] R. Deng, Q. Li, P. Wang, Q. Zheng, Y. Huo, F. Xie, D. Lin, Metal-organic framework derived core-shell structured cu-doped Co0. 85Se@ NC@ C microcubes as advanced anodes for sodium-ion batteries, Electrochim. Acta 432 (2022) 141157.

[22] Z. Hao, X. Shi, Z. Yang, L. Li, S.L. Chou, Developing high-performance metal selenides for sodium-ion batteries, Adv. Funct. Mater. 32 (51) (2022) 2208093.

[23] J. Li, W. Zhang, W. Zheng, Metal selenides find plenty of space in architecting advanced sodium/potassium ion batteries, Small 2305021 (2023).

[24] Z. Li, L. Yu, X. Tao, Y. Li, L. Zhang, X. He, Y. Chen, S. Xiong, W. Hu, J. Li, Honeycomb-structured MoSe2/rGO composites as high-performance anode materials for sodium-ion batteries, Small 2304124 (2023).

[25] W. Zhu, A. Li, Z. Wang, J. Yang, Y. Xu, Metal–organic frameworks and their derivatives: designing principles and advances toward advanced cathode materials for alkali metal ion batteries, Small 17 (22) (2021) 2006424.

[26] I.-S. Hwang, Y.-H. Lee, J.-M. Yoon, Y. Hwa, C.-M. Park, GaSb nanocomposite: new high-performance anode material for na-and K-ion batteries, Compos. B Eng. 243 (2022) 110142.

[27] Y. Jiang, M. Xie, F. Wu, Z. Ye, Y. Zhang, Z. Wang, Y. Zhou, L. Li, R. Chen, Cobalt selenide hollow polyhedron encapsulated in graphene for high-performance lithium/sodium storage, Small 17 (40) (2021) 2102893.

[28] H. Fan, H. Yu, Y. Zhang, J. Guo, Z. Wang, H. Wang, N. Zhao, Y. Zheng, C. Du, Z. Dai, 1D to 3D hierarchical iron selenide hollow nanocubes assembled from FeSe2@ C core-shell nanorods for advanced sodium ion batteries, Energy Storage Mater. 10 (2018) 48–55.

[29] Y. Xiao, Y. Miao, S. Wan, Y.K. Sun, S. Chen, Synergistic engineering of se vacancies and Heterointerfaces in zinc-cobalt selenide anode for highly efficient na-ion batteries, Small 18 (28) (2022) 2202582.

[30] Z. Kong, L. Wang, S. Iqbal, B. Zhang, B. Wang, J. Dou, F. Wang, Y. Qian, M. Zhang, L. Xu, Iron selenide-based heterojunction construction and defect engineering for fast potassium/sodium-ion storage, Small 18 (15) (2022) 2107252.

[31] Q. Li, R. Deng, Y. Chen, J. Gong, P. Wang, Q. Zheng, Y. Huo, F. Xie, X. Wei, C. Yang, Homologous heterostructured NiS/NiS2@ C hollow ultrathin microspheres with Interfacial electron redistribution for high-performance sodium storage, Small 2303642 (2023).

[32] H. Zhu, Z. Li, F. Xu, Z. Qin, R. Sun, C. Wang, S. Lu, Y. Zhang, H. Fan, Ni_3Se_4@ $CoSe_2$ hetero-nanocrystals encapsulated into CNT-porous carbon interpenetrating frameworks for high-performance sodium ion battery, J. Colloid Interface Sci. 611 (2022) 718–725.

[33] S. Zhang, L. Sun, L. Yu, G. Zhai, L. Li, X. Liu, H. Wang, Core–shell CoSe2/WSe2 heterostructures@ carbon in porous carbon nanosheets as advanced anode for sodium ion batteries, Small 17 (49) (2021) 2103005.

[34] R. Deng, P. Wang, Y. Chen, Q. Zheng, D. Lin, NiS_2/CoS_2@ NC@ C nanocubes derived from prussian blue analogues as an advanced anode with extraordinary long-cycle performance for sodium ion batteries, Electrochim. Acta 469 (2023) 143245.

[35] Y.B. Kim, H.Y. Seo, K.H. Kim, J.S. Cho, Y.C. Kang, G.D. Park, Synthesis of iron sulfide nanocrystals encapsulated in highly porous Carbon-coated CNT microsphere as anode materials for sodium-ion batteries, Small 2305686 (2023).

[36] S. Chen, S. Huang, J. Hu, S. Fan, Y. Shang, M.E. Pam, X. Li, Y. Wang, T. Xu, Y. Shi, Boosting sodium storage of $Fe_{1-x}S/MoS_2$ composite via heterointerface engineering, Nano-Micro Letters 11 (2019) 1–14.

[37] Q. Li, P. Wang, Y. Chen, X. Liao, R. Deng, Q. Zheng, D. Lin, Prussian blue-derived multiple yolk–single shell-structured se-doped Fe_{78}@ NC@ C microcube composites as high-rate anodes for sodium-ion batteries, Inorg. Chem. Front. 10 (20) (2023) 6105–6115.

[38] H. Shan, J. Qin, Y. Ding, H.M.K. Sari, X. Song, W. Liu, Y. Hao, J. Wang, C. Xie, J. Zhang, Controllable heterojunctions with a semicoherent phase boundary boosting the potassium storage of $CoSe_2/FeSe_2$, Adv. Mater. 33 (37) (2021) 2102471.

[39] Z. Lv, B. Peng, X. Lv, Y. Gao, K. Hu, W. Dong, G. Zheng, F. Huang, Intercalative motifs-induced space confinement and bonding covalency enhancement enable ultrafast and Large sodium storage, Adv. Funct. Mater. 33 (16) (2023) 2214370.

[40] H. Li, Y. He, Q. Wang, S. Gu, L. Wang, J. Yu, G. Zhou, L. Xu, SnSe2/NiSe2@N-doped Carbon yolk-Shell heterostructure construction and selenium vacancies engineering for ultrastable sodium-ion storage, Adv. Energy Mater. 13 (47) (2023) 2302901.

[41] P. Wang, Y. Chen, X. Liao, Q. Zheng, R. Zhao, K.-H. Lam, D. Lin, Boosting the sodium storage performance of iron selenides by a synergetic effect of vacancy engineering and spatial confinement, J. Colloid Interface Sci. 655 (2024) 748–759.

[42] R. Deng, Q. Li, P. Wang, Q. Zheng, Y. Huo, F. Xie, D. Lin, Metal-organic framework derived core-shell structured cu-doped $Co_{0.85}Se$@NC@C microcubes as advanced anodes for sodium-ion batteries, Electrochim. Acta 432 (2022) 141157.

[43] S. Xiao, X. Li, W. Zhang, Y. Xiang, T. Li, X. Niu, J.S. Chen, Q. Yan, Bilateral Interfaces in In_2Se_3-$CoIn_2$-$CoSe_2$ heterostructures for high-rate reversible sodium storage, ACS Nano 15 (8) (2021) 13307–13318.

[44] J. Feng, S.H. Luo, S.X. Yan, Y. Zhan, Q. Wang, Y.H. Zhang, X. Liu, L.J. Chang, Hierarchically nitrogen-doped carbon wrapped $Ni_{0.6}Fe_{0.4}Se_2$ binary-metal selenide nanocubes with extraordinary rate performance and high pseudocapacitive contribution for sodium-ion anodes, J. Mater. Chem. A 9 (2021) 1610–1622.

[45] J. Feng, S.H. Luo, S.X. Yan, Y. Zhan, Q. Wang, Y.H. Zhang, X. Liu, L.J. Chang, Rational Design of Yolk–Shell Zn-Co-Se@N-Doped Dual Carbon Architectures as Long-Life and High-Rate Anodes for Half/Full Na-Ion Batteries, Small 17(46) 2101887.

[46] J. Feng, S.H. Luo, Y. Zhan, S.X. Yan, P.W. Li, L. Zhang, Q. Wang, Y.H. Zhang, X. Liu, Ingeniously designed Yolk–Shell-structured $FeSe_2$@NDC nanoboxes as an excellent long-life and high-rate anode for half/full na-ion batteries, ACS Appl. Mater. Interfaces 13 (43) (2021) 51095–51106.

[47] J. Feng, S.H. Luo, Y.C. Lin, Y. Zhan, S.X. Yan, P.Q. Hou, Q. Wang, Y.H. Zhang, Metal-organic framework derived $CoSe_2$/N-doped carbon core-shell nanoparticles encapsulated in porous N-doped carbon nanotubes as high-performance anodes for sodium-ion batteries, J. Power Sources 535 (2022) 231444.

[48] Z.-R. Zhang, S.-H. Luo, J.-C. Wang, M.-Y. Sun, S.-X. Yan, Q. Wang, Y.-H. Zhang, X. Liu, X.-F. Lei, Optimization of preparation of lignite-based activated carbon for high-performance supercapacitors with response surface methodology, J. Storage Mater. 56 (2022) 105913.

[49] Y. Rao, J. Wang, P. Liang, Heterostructured WS_2/MoS_2@carbon hollow microspheres anchored on graphene for high-performance Li/Na storage, Chem. Eng. J. 443 (2022) 136080.

[50] J. Liu, S. Xiao, X. Li, Z. Li, X. Li, W. Zhang, Y. Xiang, X. Niu, J.S. Chen, Interface engineering of Fe_3Se_4/FeSe heterostructure encapsulated in electrospun carbon nanofibers for fast and robust sodium storage, Chem. Eng. J. 417 (2021) 129279.

[51] B. Li, Y. Liu, X. Jin, S. Jiao, G. Wang, B. Peng, S. Zeng, L. Shi, J. Li, G. Zhang, Sodium-ion batteries: designed formation of hybrid nanobox composed of Carbon sheathed CoSe2 anchored on nitrogen-doped Carbon skeleton as ultrastable anode for sodium-ion batteries (small 42/2019), Small 15 (42) (2019) 1970227.

[52] X. Liu, L. Yang, G. Xu, J. Cao, Pomegranate-like porous $NiCo_2Se_4$ spheres with N-doped carbon as advanced anode materials for Li/Na-ion batteries, Green Energy Environ. 7 (3) (2022) 554–565.

[53] Y. Chen, Q. Li, P. Wang, X. Liao, J. Chen, X. Zhang, Q. Zheng, D. Lin, K.h. Lam, High-Energy-Density Cathode Achieved via the Activation of a Three-Electron Reaction in Sodium Manganese Vanadium Phosphate for Sodium-Ion Batteries, Small (2023) 2304002.

[54] R. Fan, C. Zhao, J. Ma, J. Wu, T. He, Y. Dong, J. Dai, Y. Cai, Rich self-generated phase Boundaries of heterostructured VS4/Bi2S3@ C nanorods for long lifespan sodium-ion batteries, Small 18 (45) (2022) 2205175.

[55] H. Zheng, J. Wang, H. Li, S. Deng, Y. Zuo, W. Yan, J. Zhang, Constructing a novel heterostructure of NiSe2/CoSe2 nanoparticles with boosted sodium storage

properties for sodium-ion batteries, J. Mater. Chem. A 10 (30) (2022) 16268–16279.
[56] J. Je, H. Lim, H.W. Jung, S.O. Kim, Ultrafast and ultrastable heteroarchitectured porous nanocube anode composed of CuS/FeS2 embedded in nitrogen-doped carbon for use in sodium-ion batteries, Small 18 (6) (2022) 2105310.
[57] D. Qiu, A. Gao, W. Zhao, Z. Sun, B. Zhang, J. Xu, T. Shen, J. Wang, Z. Fang, Y. Hou, Fast-Charging degradation mechanism of two-dimensional FeSe anode in sodium-ion batteries, ACS Energy Lett. 8 (10) (2023) 4052–4060.
[58] K. Zhang, M. Park, L. Zhou, G.H. Lee, W. Li, Y.M. Kang, J. Chen, Urchin-like CoSe2 as a high-performance anode material for sodium-ion batteries, Adv. Funct. Mater. 26 (37) (2016) 6728–6735.
[59] Y. Zhang, L. Cheng, L. Li, Y. Lin, S. Li, Y. Li, X. Ren, P. Zhang, L. Sun, ZnSe/SnSe heterostructure incorporated with selenium/nitrogen co-doped Carbon nanofiber skeleton for sodium-ion batteries, Small 2306536 (2024).
[60] F. Huang, L. Wang, D. Qin, Z. Xu, M. Jin, Y. Chen, X. Zeng, Z. Dai, Constructing heterostructured Bimetallic selenides on an N-doped Carbon nanoframework as anodes for ultrastable na-ion batteries, ACS Appl. Mater. Interfaces 14 (1) (2022) 1222–1232.
[61] S.A. He, Z. Cui, Q. Liu, G. He, D.J.L. Brett, W. Luo, R. Zou, M. Zhu, Enhancing the electrochemical performance of sodium-ion batteries by building optimized NiS2/NiSe2 heterostructures, Small 17 (45) (2021).